

PCCP

Accepted Manuscript



This is an *Accepted Manuscript*, which has been through the Royal Society of Chemistry peer review process and has been accepted for publication.

Accepted Manuscripts are published online shortly after acceptance, before technical editing, formatting and proof reading. Using this free service, authors can make their results available to the community, in citable form, before we publish the edited article. We will replace this *Accepted Manuscript* with the edited and formatted *Advance Article* as soon as it is available.

You can find more information about *Accepted Manuscripts* in the [Information for Authors](#).

Please note that technical editing may introduce minor changes to the text and/or graphics, which may alter content. The journal's standard [Terms & Conditions](#) and the [Ethical guidelines](#) still apply. In no event shall the Royal Society of Chemistry be held responsible for any errors or omissions in this *Accepted Manuscript* or any consequences arising from the use of any information it contains.

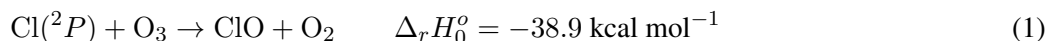
The Cl+O₃ reaction: A detailed QCT simulation of molecular beam experiments

M. Menéndez,^a J. F. Castillo,^a B. Martínez Haya,^b and F. J. Aoiz^{a*}

We have studied in detail the dynamics of the Cl+O₃ reaction in the 1-56 kcal mol⁻¹ collision energy range using quasi-classical trajectory calculations (QCT) on a recent potential energy surface (PES) [J. F. Castillo *et al.*, *Phys. Chem. Chem. Phys.*, 2011, **13**, 8537]. The main goal of this work has been to assess the accuracy of the PES and the reliability of the QCT method by comparison with the existing crossed molecular beam results [J. Zhang and Y. T. Lee *J. Phys. Chem. A*, 1997, **101**, 6485]. For this purpose, we have developed a methodology that allows us to determine the experimental observables in crossed molecular beam experiments (integral and differential cross sections, recoil velocity distributions, scattering angle-recoil velocity polar maps, etc.) as continuous functions of the collision energy. Using these distributions, raw experimental data in the laboratory frame (angular distributions and time-of-flight spectra) have been simulated from first principles with the sole information of the instrumental parameters and taking into account the energy spread. It has been found a general good agreement with the experimental data, thereby demonstrating the adequacy of the QCT method and the quality of the PES to describe the dynamics of this reaction at the level of resolution of the existing crossed beam experiments. Some features which are apparent in the differential cross sections have also been analysed in terms of the dynamics of the reaction and its evolution with the collision energy.

1 Introduction

The reaction



is considered to play a key role in the catalytic O₃ depletion cycles in the stratosphere.¹ Nowadays, there is general consensus that the catalytic cycle which involves the formation of (ClO)₂ dimers is the responsible for most of the O₃ destruction in the Antarctic stratosphere.^{2,3} The first few theoretical studies of the electronic structure ClO₃ reactive system were performed in the 90's.⁴⁻⁷ Those previous studies were aimed to characterize the stationary points along the reaction path but the main conclusions were found to be somewhat puzzling. In particular, the transition state (TS) geometry and the height of the barrier were found to be quite at variance from study to study. For instance, whereas Huang and Mebel⁶ predicted a barrier for the reaction of about 4-5 kcal mol⁻¹ and a non-planar TS configuration, the calculations carried out by Tyrell *et al.*⁷ suggested a barrierless reaction path and a planar TS geometry. The

^a Departamento de Química Física I, Facultad de CC. Químicas, Universidad Complutense de Madrid, 28040 Madrid, Spain.

^b Department of Physical, Chemical and Natural Systems, Universidad Pablo de Olavide. ES-41013 Seville, Spain.

* Email:aoiz@quim.ucm.es

open shell character of the Cl atom as well as of the O₂ and ClO molecules, and the biradical character of the O₃ molecule make electronic structure calculations particularly challenging. Besides, the expected early-like transition state requires that the long range interactions must be calculated with great accuracy, which implies that electronic correlation has to be taken into account using high level post-Hartree-Fock methods. An early theoretical attempt to produce a global, analytical potential energy surface (PES) for reaction dynamics calculations was made by Farantos and Murrell⁸ using a many-body expansion based on empirically derived parameters. This PES exhibits an early transition state corresponding to the collinear collision pathway in which Cl attacked along the axis of one of the O–O bonds of O₃ molecule. The classical barrier height for the collinear pathway is 0.34 kcal mol⁻¹ (0.26 kcal mol⁻¹ when the zero point energies are included), consistent with the experimental activation energy of 0.1–0.5 kcal mol⁻¹ derived from the kinetic studies. As it could be expected, quasiclassical trajectory calculations (QCT) on this PES led to a rate constant at $T=300$ K of 1.34×10^{-11} cm³ s⁻¹, in accordance with the experimental value⁹ of $(1.3 \pm 0.07) \times 10^{-11}$ cm³ s⁻¹. The QCT angular distributions evaluated on the FM PES at different collision energies, E_T , from 6 to 32 kcal mol⁻¹, systematically led to reaction products scattered predominantly in the backward hemisphere, predicting a direct reaction mechanism.

Experimental derivations of the centre-of-the-mass (CM) angular distributions were achieved by the Cl+O₃ crossed molecular beam (CMB) study by Zhang and Lee¹⁰ at three CM translational (collision) energies ranging from 6 to 32 kcal mol⁻¹. Laboratory angular distributions (LAB AD) and time-of-flight (TOF) spectra of the ClO product were measured, and the corresponding CM angle-velocity (AV) differential cross sections were inferred. The ClO product was found to be sideways and forward scattered with respect to the incoming Cl atom in the CM frame. The CM angular distribution shifts to the forward hemisphere as the collision energy increases. The experimentally derived CM angular distributions could not be reproduced by the QCT calculations on the FM PES⁸. Additionally, the average translational energy of the products was found to be 35–65% of the total available energy. No evidence was found for electronically excited O₂ products and the results ruled out the formation of a long-lived complex intermediate at the collision energy range considered in the experiment. Zhang and Lee concluded that the reaction has to occur mainly through a direct abstraction mechanism. A coplanar attack by the chlorine on a terminal oxygen of the ozone was proposed to account for the wide angular range of backward scattered products. The presence of a narrower range of sideways-forward scattered products was tentatively interpreted as arising from out-of-plane collisions. These experimental findings were looking forward to a full theoretical account by accurate *ab initio* calculations of the PES and corresponding dynamical calculations.

Only recently, a global, fully *ab initio* PES (hereinafter CAM10) has been calculated and employed in dynamical calculations.^{11,12} The CAM10 PES was constructed using the interpolation method, proposed by Collins and coworkers,¹³ of *ab initio* points computed with Unrestricted Quadratic Configuration Interaction with Single and Double excitations (UQCISD) and aug-cc-pVDZ basis set. The QCT calculations on the CAM10 PES managed to reproduce quite well the total center-of-the-mass differential cross sections (DCSs) extracted from the analysis of the CMB experiments by Zhang and Lee.¹⁰ QCT calculations of rate coefficients in the 200–400K temperature range were found to lead to somewhat lower values below 300 K than the recommended experimental ones, once a correction for the spin-orbit splitting was introduced.^{11,12} However, calculations of rate coefficients in the same range of

temperatures using Ring Polymer Molecular Dynamics^{14,15} on the CAM10 PES were found to be in good agreement with the experimental measurements.¹²

In this work we present a detailed comparison of the raw experimental data in the LAB frame,¹⁰ that is, LAB AD and TOF distributions of the ClO product, with the corresponding theoretical simulations using the angle-velocity triple differential cross sections averaged over the distribution of initial collision energies. From the methodological side, the novelty of this work is that the QCT results have been obtained sampling continuously the collision energy in the whole range of collision energies (1–56 kcal mol⁻¹). This allows us to determine the dynamical observables as a continuous function of collision energy and hence to take fully into account the energy spread of the experimental results.

The paper is structured as follows. Section 2 contains the details of the QCT calculations (section 2.1), the method to determine the triple angle-velocity (TAV) distributions as a function of the collision energy (section 2.2) and simulation of the experimental results in the LAB frame (section 2.3). Section 3 presents a detailed account of the energy dependence of the various observables as well as the comparison between the experimental and simulated results, while Section 4 presents a dynamical explanation of some of the features observed in the DCS. Finally, in section 5 the most salient conclusion of this work are exposed.

2 Methodology

2.1 Details of the Quasi-classical trajectory calculations

The general methodology of the QCT calculation is the same as in previous works. It is described more extensively in refs. 11,16–18, and only the particular details relevant to the present work will be given here.

The present calculations have been performed using the full dimensional, global, analytical CAM10 PES.¹¹ This PES was calculated using the GROW package^{13,19–21} by interpolation of quantum chemistry data. The *ab initio* calculations, at the level of the UQCISD/aug-cc-pVDZ method, and the comparison with other methods are discussed in ref. 11 where the reader is referred to for further details.

Two different series of QCT calculations have been carried out in this work. In the first series, batches of trajectories were run at 15 discrete, specific collision (translational) energies, E_T , ranging from 1 kcal mol⁻¹ to 42 kcal mol⁻¹. In all, 4.5 million of trajectories were calculated in this series. The second series of calculations was performed by varying randomly the collision energy for each trajectory in the 1 to 56 kcal mol⁻¹ range. Since the maximum impact parameter at each collision energy, $b_{\max}(E_T)$, decreases rapidly with E_T , the impact parameter b for each trajectory was sampled by taking into account the dependence of b_{\max} with E_T . This dependence was previously determined with the batches of trajectories run a fixed E_T . Once the value of E_T is randomly sampled for each trajectory, the value of b is sampled as $b = \xi^{1/2} b_{\max}(E_T)$, where ξ is a random number in the [0, 1] interval. Each trajectory is then weighted with $w_i = b_{\max}^2(E_T)/D^2$, where $D=5.5$ Å is the absolute maximum impact parameter in the whole calculation. Three batches of 10⁶ trajectories each were run covering different ranges of collision energies, such that the three of them span the whole interval, 1–56 kcal mol⁻¹ necessary to simulate the data from the cross molecular beam experiment by Zhang and Lee.¹⁰

The initial distance R_{\max} from the Cl atom to the nearest terminal O atom of the O_3 molecule was set to 8 Å. Integration of the equations of motion was carried out using an adapted version of the VENUS96 program²² with a time step of 0.04 fs. The typical conservation of energy was better than 1 in 10^5 . The initial conditions for the O_3 molecule in its ground vibrational state have been chosen using the microcanonical normal mode sampling as implemented in the VENUS96 code. The rotational energy was assigned using the value of $3/2 (k_B T_{\text{rot}})$ corresponding to the classical equipartition of the energy at $T = T_{\text{rot}}$. All the calculations were carried out at a rotational temperature of $T_{\text{rot}}=100$ K, which is a good estimate of the O_3 rotational temperature in the conditions of the molecular beam experiment of Zhang and Lee.¹⁰ In turn, the assignment of diatomic products quantum numbers has been carried out as in previous works, calculating the rovibrational levels of ClO and O_2 by the semiclassical quantization of the classical action using in each case the asymptotic diatomic potentials of the PES. The classical rotational angular momenta are equated to $[j'(j' + 1)]^{1/2}\hbar$ rounding the (real) j' value so obtained to the nearest integer. The vibrational quantum number is found by Einstein-Brillouin-Keller (EBK) semiclassical quantization of the action integral.²² Given the relatively small vibrational quanta of both molecular products, the correction with the Gaussian binning method was found to be unnecessary.

2.2 Determination of the angle-velocity distributions

In the experimental article by Zhang and Lee,¹⁰ it was shown that the scattering angle-recoil velocity distributions change noticeably with the collision energy, as it will be theoretically verified hereunder. Therefore, for an accurate simulation of the experimental quantities measured in the experiment it is necessary to take into account the spread of collision energies for each of the three nominal collision energies at which the experiments were performed. To this end, we have developed in this work a general method that allows the simultaneous fit of the dependence of the reaction cross section on three quantities: translational collision energy, scattering angle, and recoil velocity. The goal is thus to determine the triple angle-velocity differential cross sections (TAV-DCSs) as a function of collision energy as precisely as possible, and with an efficient algorithm that allows to retrieve its value every time is needed in the simulation of the angular and time-of-flight distribution in the LAB frame. The procedure is an extension of that developed previously to determine the TAV-DCS at a single (fixed) collision energy.^{23,24}

The method can be described as follows. As shown in ref. 23, the excitation function, that is, the reaction cross section as a function of the relative translational (or collision) energy, $\sigma_R(E_T)$, is calculated as a moment expansion in Legendre polynomials, $P_k(y)$, using the reduced variable $y \in [-1, 1]$

$$y = \frac{2E_T - E_2 - E_1}{\Delta E}, \quad (2)$$

where E_1 and E_2 are the minimum and maximum collision energy where the trajectories have been calculated and $\Delta E = E_2 - E_1$. In the present case $E_1=1$ kcal mol⁻¹, and $E_2=56$ kcal mol⁻¹.

The expression of the $\sigma_R(E_T)$ truncated in k_{\max} is given by

$$\sigma_R(E_T) = \frac{2Q}{\Delta E} \sum_{k=0}^{k_{\max}} b_k P_k(y) = \frac{2Q}{\Delta E} \rho[y(E_T)] \quad (3)$$

where Q is the Monte Carlo estimate of the integral

$$Q = \langle \sigma_{\text{R}}(E_{\text{T}}) \rangle \Delta E \approx \pi D^2 \Delta E \frac{S_{\text{w}}}{N_{\text{tot}}}, \quad (4)$$

being N_{tot} the total (reactive and non-reactive) number of trajectories and S_{w} the sum of the weights of the reactive trajectories,

$$S_{\text{w}} = \sum_{i=1}^{N_{\text{R}}} w_i \quad (5)$$

where w_i is the weight of the i -th trajectory. The coefficients of the Legendre expansion, b_k , of eqn. (3) are calculated as the Monte Carlo average of Legendre moments

$$b_k = \frac{[k]}{S_{\text{w}}} \sum_{i=1}^{N_{\text{R}}} w_i P_k(y_i) \quad (6)$$

where $[k] \equiv (2k + 1)/2$ and similarly for other integer numbers.

TAV-DCSs, $d^3\sigma_{\text{R}}/d\omega dw'$, were determined by fitting to a triple series of Legendre polynomials in reagent translational energy, E_{T} , scattering angle, $\cos \theta$, and recoil velocity, w' , of the detected product, in this case, ClO. The resulting expression is

$$\frac{d^3\sigma_{\text{R}}}{d\omega dw'}(E_{\text{T}}) = \frac{\sigma_{\text{R}}(E_{\text{T}})}{2\pi} \frac{2}{w'_{\text{max}} - w'_{\text{min}}} \sum_n \sum_m \alpha_{nm}(E_{\text{T}}) P_n[r(w')] P_m(\cos \theta) \quad (7)$$

The reduced recoil velocity, r , defined in the $[-1, 1]$ interval is given by

$$r = \frac{2w' - w'_{\text{max}} - w'_{\text{min}}}{w'_{\text{max}} - w'_{\text{min}}} \quad (8)$$

and w'_{max} and w'_{min} are the maximum and minimum recoil velocities of the detected product. Usually $w'_{\text{min}} = 0$.

The collision energy dependent coefficients, $\alpha_{nm}(E_{\text{T}})$, of eqn. (7) are given by

$$\alpha_{nm}(E_{\text{T}}) = \frac{1}{\rho[y(E_{\text{T}})]} \sum_{k=0} \eta_{knm} P_k[y(E_{\text{T}})] \quad (9)$$

where y and $\rho[y(E_{\text{T}})]$ are defined in eqn. (2) and eqn. (3), respectively. The triple indexed coefficients, η_{knm} , can be calculated as

$$\begin{aligned} \eta_{knm} &= \frac{[k][n][m]}{S_{\text{w}}} \sum_{i=1}^{N_{\text{R}}} w_i P_k(y_i) P_n(r_i) P_m(\cos \theta_i) \\ &= [k][n][m] \langle P_k(y) P_n(r) P_m(\cos \theta) \rangle_{N_{\text{R}}} \end{aligned} \quad (10)$$

where y_i , r_i and $\cos \theta_i$ are the reduced collision energy, eqn (2), reduced recoil velocity and the cosine of the scattering angle corresponding to the i -th trajectory. Hence these coefficients are the average over the ensemble of N_{R} reactive trajectories of the product of the Legendre polynomials of degree k , n , and m for the respective variables. In particular,

$$\eta_{k00} = \frac{1}{4} \frac{[k]}{S_{\text{w}}} \sum_{i=1}^{N_{\text{R}}} w_i P_k(y_i) = \frac{1}{4} b_k \quad (11)$$

Substituting eqn. (3) and eqn. (9) in eqn. (7), the triple angle-velocity distribution can be also written as

$$\frac{d^3\sigma_{\text{R}}}{d\omega dw'}(E_{\text{T}}) = \frac{2Q}{\Delta E} \frac{1}{2\pi} \frac{2}{w'_{\text{max}}} \sum_{k=0}^{k_{\text{max}}} \sum_{n=0}^{n_{\text{max}}} \sum_{m=0}^{m_{\text{max}}} \eta_{knm} P_k(y) P_n(r) P_m(\cos\theta) \quad (12)$$

Integrating eqn. (7) over w' , one obtains the expression of the differential cross section as a function of the collision energy

$$\begin{aligned} \frac{d^2\sigma_{\text{R}}}{d\omega}(E_{\text{T}}) &= \frac{\sigma_{\text{R}}(E_{\text{T}})}{2\pi} \sum_m 2\alpha_{0m}(E_{\text{T}}) P_m(\cos\theta) \\ &= \frac{2Q}{\Delta E} \frac{1}{2\pi} \sum_{k=0}^{k_{\text{max}}} \sum_{m=0}^{m_{\text{max}}} 2\eta_{k0m} P_k[y(E_{\text{T}})] P_m(\cos\theta) \end{aligned} \quad (13)$$

If instead eqn. (7) is integrated over $\cos\theta$ and ϕ , and the result is divided by $\sigma_{\text{R}}(E_{\text{T}})$, the expression of dependence of the recoil velocity distribution with the collision energy, *i. e.*, the conditional recoil velocity distribution, $P_{\text{R}}(w'|E_{\text{T}})$, is recovered,

$$\begin{aligned} P_{\text{R}}(w'|E_{\text{T}}) &= \frac{1}{\sigma_{\text{R}}(E_{\text{T}})} \frac{d\sigma_{\text{R}}}{dw'} = \frac{2}{w'_{\text{max}}} \sum_n 2\alpha_{n0}(E_{\text{T}}) P_n[r(w')] \\ &= \frac{2}{w'_{\text{max}}} \frac{1}{\rho[y(E_{\text{T}})]} \sum_{k=0}^{k_{\text{max}}} \sum_{n=0}^{n_{\text{max}}} 2\eta_{kn0} P_k[y(E_{\text{T}})] P_n[r(w')] \end{aligned} \quad (14)$$

In the second lines of eqn. (13) and eqn. (14), the coefficients α_{0m} and α_{n0} have been substituted by their expressions according to eqn. (9).

Similarly, the expression of the conditional distribution of the product's translational energy, E'_{T} , at a given translational collision energy, E_{T} , can be written as

$$P_{\text{R}}(E'_{\text{T}}|E_{\text{T}}) = P[r(E'_{\text{T}})|E_{\text{T}}] \frac{dr}{dE'_{\text{T}}} = \frac{1}{(E'_{\text{max}} \cdot E_{\text{T}})^{1/2}} \sum_n 2\alpha_{n0}(E_{\text{T}}) P_n[r(E'_{\text{T}})] \quad (15)$$

where

$$E'_{\text{max}} = \frac{1}{2} \frac{m_{\text{ClO}} M}{m_{\text{O}_2}} (w'_{\text{max}})^2 \quad (16)$$

is the maximum product's translational energy in the whole set of energy dependent trajectories and $M = m_{\text{ClO}} + m_{\text{O}_2}$.

In the case of fixed collision energy calculations, the DCS, recoil velocity distribution in the CM frame, and TAV-DCS for fixed collision energy have been determined with the expressions given elsewhere^{18,23,24} and they will not be repeated here. Suffice it to say that a one-dimensional expansion in Legendre polynomials was used for the fit of the DCSs and recoil velocity distributions in terms of $\cos\theta$ and the reduced recoil velocity $r = (2w'/w'_{\text{max}} - 1)$, respectively. The Smirnov–Kolmogorov test comparing the cumulative probability distributions was used to decide where the series could be truncated. Significance levels higher than 99% could be achieved using 10-20 Legendre moments, ensuring a very good convergence, such that the inclusion of more terms does not produce any significant change. The error bars, calculated as in ref. 25, correspond to plus/minus two standard deviations. Similarly, the

TAV-DCS was fitted using a two-dimensional Legendre expansion in the same variables as described in detail in refs. 23 and 24. The double series was truncated in the same number of coefficients as that used in the fit of the one-dimensional distributions.

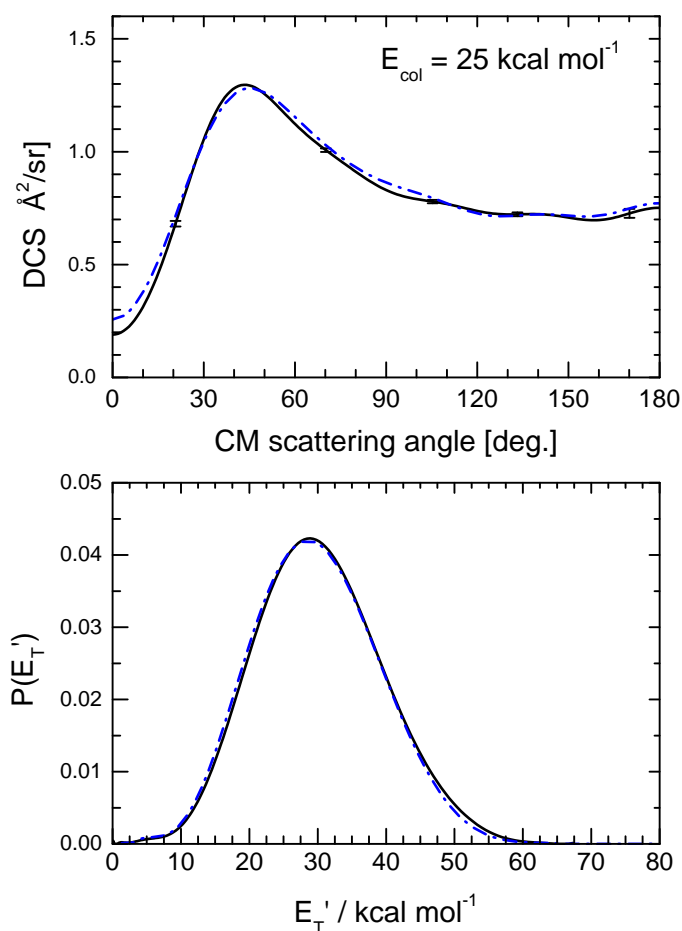


Fig. 1 Comparison of differential cross section (top) and product translational energy distribution (bottom) at $E_T = 25 \text{ kcal mol}^{-1}$ calculated using a batch of trajectories at fixed collision energy (black solid line) and that resulting of the calculation using the batches of trajectories in which the the collision energy is sampled for each trajectory in the 1-56 kcal mol^{-1} collision energy interval (blue dash-dot line).

At this point, it is appropriate to test the accuracy of the distributions calculated with the methodology of section 2.2 based on trajectories uniformly sampled in the whole range of collision energy with the results derived from batches of trajectories run at fixed collision energy. The comparison between the two sets of results is illustrated in Fig. 1 for the DCS and product translational energy distribution at 25 kcal mol^{-1} . In the case of variable energy calculations, this value of E_T was substituted in the triple expansions eqn (13) and eqn (14).

As can be seen, the agreement is excellent within the statistical error bars of each distribution. Even more stringent is the comparison between the angle-recoil velocity polar maps, shown in Fig. 2, for which the agreement is also excellent.

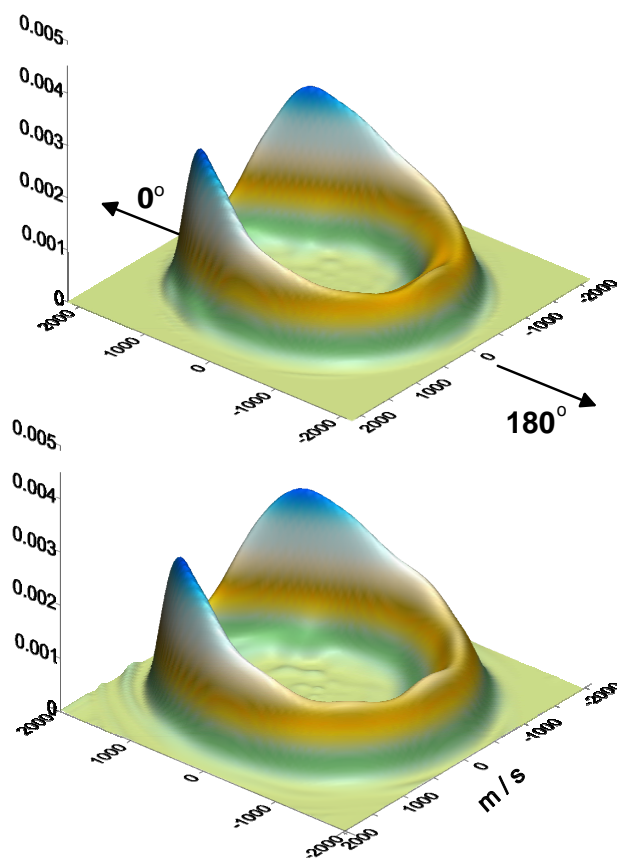


Fig. 2 Scattering angle/recoil velocity polar map of the triple differential cross-sections at $E_T = 25 \text{ kcal mol}^{-1}$, where the results from calculations at fixed collision energy (top) and those using variable collision energy (bottom) are compared. The radial and angular coordinates represent the modulus of the recoil velocity (in m s^{-1}) and the scattering angle, respectively.

2.3 Simulation of the experimental results in the laboratory frame

Simulation of the LAB AD of scattered ClO molecules is carried out by transforming the theoretical CM TAV-DCSs into the LAB system.²⁶ The signal at an angle Θ can be expressed as

$$I(\Theta_{\text{LAB}}) = \int n_1(\mathbf{r})n_2(\mathbf{r})d^3\mathbf{r} \int D(\Omega)d\Omega \times \iint f(v_1)f(v_2)v_r dv_1 dv_2 \int \left(\frac{d^3\sigma_{\text{R}}}{d\omega dw'} \right) \frac{v'}{w'^2} dv' \quad (17)$$

where $n_1(\mathbf{r})$ and $n_2(\mathbf{r})$ are the spatial beam densities, $f(v_1)$ and $f(v_2)$ are the reagent beam velocity distributions, v_r is the reagent relative velocity, $D(\Omega)$ function accounts for the detector aperture, and v'/w'^2 is the Jacobian of the CM to LAB transformation for product density detection. The calculation procedure is similar to the one described previously.^{27–29} The experimental parameters for the simulation were taken from ref. 10.

The TOF spectra were simulated in a similar way.^{28,29} Thus, the signal at a given time t and LAB angle Θ_{LAB} can

be expressed as

$$I_{\text{LAB}}(t; \Theta_{\text{LAB}}) = \int n_1(\mathbf{r})n_2(\mathbf{r})d^3\mathbf{r} \int D(\Omega)d\Omega \times \\ \times \int \int f(v_1)f(v_2)v_r dv_1 dv_2 \int_{t-\tau/2}^{t+\tau/2} \left(\frac{d^3\sigma_{\text{R}}}{d\omega dw'} \right) \frac{v'}{w'^2} \frac{L}{t'^2} dt' \quad (18)$$

where L is the flight length, t the corresponding time of flight of the formed product, and the factor L/t'^2 accounts for the transformation from velocity to time space. The experimental L was set at 30.1 cm and the channel width was taken to be $5\mu\text{s}$.¹⁰

2.4 Classical Reactive Deflection Function

Within the QCT framework, it is possible to determine the joint dependence of the reaction probability as a function of the orbital angular momentum, ℓ , (or impact parameter, b) and the scattering angle, θ . It must be taken into account that the deflection function is an ill-defined concept in QM as the angular distribution depends on the coherences between the different values of the orbital angular momentum caused by the cross terms in the expansion of partial waves. However, in most cases, the coherences between groups with different ℓ values are usually not relevant, and the analysis of the deflection functions reveals a strong correlation of the various features in each DCS with specific ranges of ℓ . This is the most common behaviour for direct reactive collisions, where we find an almost one-to-one correspondence between θ and ℓ such that low (high) impact parameters correlate with high (low) scattering angles.²⁵

The double orbital angular momentum–scattering angle reaction probability can be expressed in terms of Legendre polynomials

$$P_r(\ell, \theta) = \frac{2S_{\text{w}}}{N_{\text{tot}}} \sum_m \sum_n a_{mn} P_m(\cos \theta) P_n[z(\ell)] \quad (19)$$

where S_{w} is the sum of the weights, eqn (5) and $z(\ell)$ is given by

$$z(\ell) = \frac{2\ell(\ell + 1)}{\ell_{\text{max}}(\ell_{\text{max}} + 1)} - 1 \quad (20)$$

and the a_{mn} coefficients are given by

$$a_{mn} = \frac{[m][n]}{S_{\text{w}}} \sum_{i=1}^{N_{\text{R}}} w_i P_m(\cos \theta_i) P_n(z_i)$$

Instead of plotting $P_r(\ell, \theta)$, it is more appropriate to use a probability density function given by

$$D_r(\ell, \theta) = \frac{2\pi}{\sigma_{\text{R}}} \frac{1}{2k_{\text{in}}^2} (2\ell + 1) P_r(\ell, \theta) \sin \theta \quad (21)$$

where k_{in} is the wavenumber vector, $k_{\text{in}} = (2\mu E_{\text{T}})^{1/2}/\hbar$. Integration of eqn (21) over ℓ and θ is equal to one.

Instead of using an expansion in Legendre polynomials, the results can be fitted to a deflection function expressed as a sum of Gaussian functions given by

$$D_r(\ell, \theta) = \frac{1}{S_{\text{w}}} \sum_{i=1}^{N_{\text{R}}} w_i G(\ell - \ell_i) G(\theta - \theta_i) \quad (22)$$

where ℓ_i and θ_i represent the values of ℓ and θ for the i -th trajectory. $G(\ell - \ell_i)$ and $G(\theta - \theta_i)$ denote normalized Gaussian functions with width parameters σ_ℓ and σ_θ , centred in ℓ_i and θ_i , respectively. The sum runs over the whole ensemble of trajectories at a given collision energy. Both methods render very similar results with essentially the same computational effort.

3 Results

Figure 3 depicts the translational (collision) energy dependence of the total reaction cross section, $\sigma_R(E_T)$, *i.e.* the excitation function, for the Cl + O₃ reaction calculated on the CAM10 PES in the collision energy range of 1–56 kcal mol⁻¹ and a rotational temperature $T_{rot}=100$ K. The continuous line, determined by means of eqn (3) using trajectories calculated by varying the collision energy, is compared with the results obtained at fixed energies given by $\sigma_R = \pi b_{max}^2 N_R/N_{tot}$, where N_R and N_{tot} are the number of reactive and total trajectories, respectively, and b_{max} is the maximum impact parameter at a given energy. As can be seen, the agreement between the two sets of results is excellent considering the substantial differences between the two procedures. This result together with those shown in Fig. 1 and Fig. 2 clearly demonstrate the reliability and accuracy of the method.

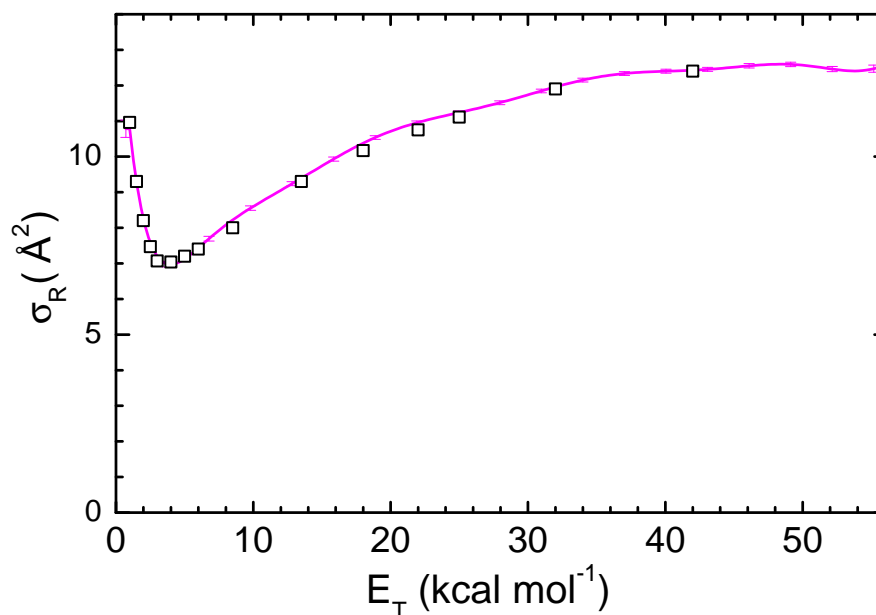


Fig. 3 Excitation function for the Cl+O₃ → O₂ + ClO reaction. QCT results on the CAM10 PES at O₃ rotational temperature $T_{rot} = 100$ K are shown. The open square symbols stand for calculations at fixed collision energy and the solid line for the results varying the collision energy in the 1–56 kcal mol⁻¹ range.

The most salient feature of the excitation function is the presence of a shallow minimum at $E_T \approx 3$ kcal mol⁻¹, followed by a smooth increase of cross section. Above 30 kcal mol⁻¹ the cross section barely changes. As discussed in a previous work,¹¹ the maximum impact parameter decreases with growing collision energy causing the decrease in the cross section at low collision energies as expected for an essentially barrierless reaction. However, beyond the minimum, the reaction probability at impact parameters below 2 Å grows rapidly while the b_{max} decreases very

slowly.¹¹ The combination of these two effects gives rise to the observed increase of the cross section. The effect of the collision energy is to make accessible in-plane configurations (recall that the transition state displays an out-of-plane configuration with a dihedral angle of 80°) and this is likely to result in an increase in the reactivity after the minimum. However, the in-plane cone of acceptance is nonetheless (see Fig. 3 of ref. 11) narrow and large impact parameters are ineffective to promote the reactivity. This explains the leveling off of the excitation functions at $E_T > 30 \text{ kcal mol}^{-1}$.

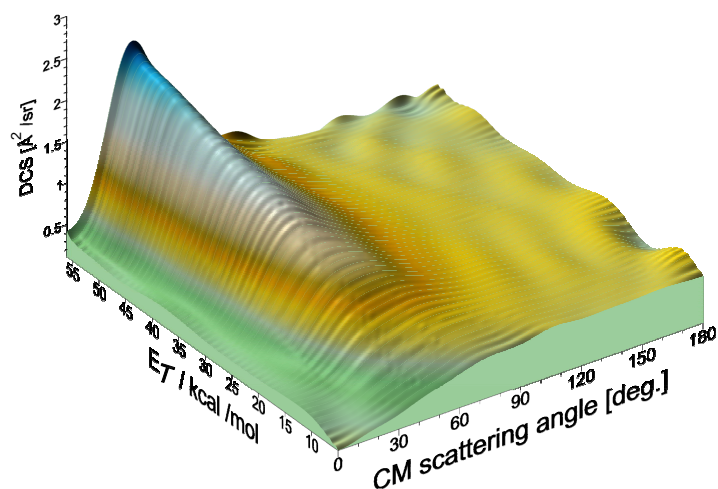


Fig. 4 Collision energy dependence of the DCSs in the $1\text{--}56 \text{ kcal mol}^{-1}$ range.

The variation of the DCS with the collision energy is depicted in the 3D plot of Fig. 4. At low collision energies the scattering is fairly isotropic in the $60^\circ\text{--}180^\circ$ angular range, and it falls rapidly below 60° . As the collision energy grows, the scattering in the forward region becomes increasingly important to the extent of forming a broad maximum at $\approx 40^\circ$ and then it drops rapidly for angles near 0° . A similar behavior is observed in the experimental results¹⁰ and previous theoretical calculations on the CAM10 PES.¹¹ The shape of the DCS and its evolution with the collision energy can be explained by resorting to the transition state geometry which features an angle $\text{Cl}\text{--}\text{O}_1\text{--}\text{O}_2$ of 109° and is slightly out of the O_3 plane. The ClO product has no hindrance to be scattered in any direction except in the forward region which is occupied by the O_2 receding molecule. As the collision energy increases, the tendency of the ClO product is to be scattered in slightly off side of the forward direction at angles $20\text{--}60^\circ$ as a consequence of the larger momentum imparted by the incoming Cl atom.

The evolution of the normalized recoil energy distribution with the collision energy is shown in Fig. 5. As can be seen, the distribution becomes wider and its maximum shifts towards higher values of E_T' with increasing collision energy. The values of the mean product's recoil energy are shown in Table 1. In spite of the displacement of $\langle E_T' \rangle$ towards higher values, the average fraction of the total energy released as translation changes only moderately with the collision energy, as also shown in Table 1, increasing from $\langle f_T \rangle = 0.36$ to $\langle f_T \rangle = 0.49$. Similarly, the standard deviation

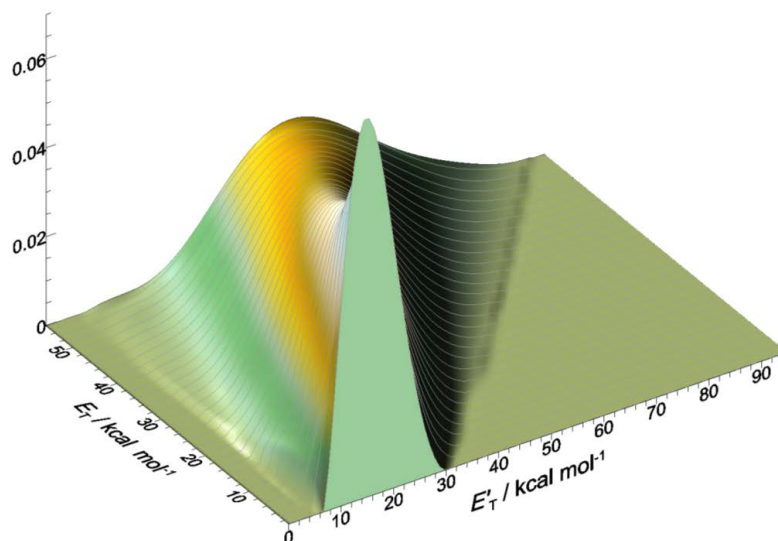


Fig. 5 Dependence of the product translational energy distribution on the collision energy in the 1-56 kcal mol⁻¹ range. At each energy the distribution is normalized to unit area according to eqn (15).

of f_T , that is, the width of the f_T distribution, barely changes through the whole range of energies here examined. Therefore, the increase of collision energy favors channeling into translation only to some extent,¹¹ indicating that there is not appreciable change in the dynamical mechanism in the studied range of collision energies.

3.1 Simulation of experimental results

This subsection will be devoted to the comparison with the crossed molecular beam results by Zhang and Lee¹⁰ using the present QCT angle-velocity DCSs calculated as a function of the collision energy. Those experiments were carried out at three nominal translational energy; namely, 6 kcal mol⁻¹, 13.5 kcal mol⁻¹, and 32 kcal mol⁻¹. The details of the experimental conditions and instrumental parameters are given in that article and, specifically, the relevant parameters of the velocity distributions of the atomic and molecular beams, and the beam divergences. Using these values, the distribution of translational (collision) energy have been calculated. In particular, the mean collision energy and the full-width-half-maximum (FWHM), as well as the maximum possible recoil velocity compatible with the energy conservation, and the average value of the reduced recoil velocity are shown in Table 2. As can be seen, the distributions are rather broad. Considering the changes in the product's angular and recoil energy distributions with the collision energy, shown in Fig. 4 and Fig. 5, respectively, it becomes evident that a faithful simulation requires the inclusion of the energy dependence of the joint scattering angle-recoil velocity distributions including the changes in the cross sections; that is, the values of the function given in eqn (7).

In what follows, we will compare the CM AV polar maps calculated at the three nominal energies with those that were derived from experiment by fitting the measured data in the LAB system with parametrized functions. Moreover, with the AV distributions as a function of the collision energy calculated according to eqn (7), we have simulated the

Table 1 Calculated mean product translational energy, $\langle E'_T \rangle$, mean fraction of the total energy released as translation, $\langle f_T \rangle$, and the variance of the f_T distribution, at several collision energies, E_T .

$E_T / \text{kcal mol}^{-1}$	$\langle E'_T \rangle / \text{kcal mol}^{-1}$	$\langle f_T \rangle$	$[\langle f_T^2 \rangle - \langle f_T \rangle^2]^{1/2}$
1.0	16.4	0.36	0.116
6.0	18.7	0.37	0.119
13.0	22.8	0.39	0.125
25.0	29.9	0.43	0.132
32.0	34.2	0.45	0.137
44.0	41.9	0.47	0.140
55.0	48.9	0.49	0.142

Table 2 Mean translational (collision) energy, full-width-half-maximum (FWHM) of the translational energy distribution, maximum possible recoil velocity, average value of the reduced product recoil velocity, $s = w'/w'_{\text{max}}$, and the standard deviation of the reduced recoil velocity distribution are shown for the three nominal experimental collision energies.¹⁰

$\langle E_T \rangle / \text{kcal mol}^{-1}$	FWHM / kcal mol ⁻¹	$w'_{\text{max}}(E_T) / \text{m s}^{-1}$	$\langle s \rangle$	$[\langle s^2 \rangle - \langle s \rangle^2]^{1/2}$
5.85	2.34	1750	0.621	0.101
13.65	7.33	1880	0.644	0.106
32.45	15.55	2170	0.666	0.107

LAB angular distributions in the three cases, as well as the ClO TOF spectra for the two highest experimental energies. The forward simulation of the observables obtained in the LAB, using the angle-velocity distributions calculated in the CM system, and its comparison with the raw experimental magnitudes constitutes the most stringent test for the results of dynamical calculations. The ultimate goal of this study is to check at the most possible detailed level the reliability of the QCT method and the PES used in the present calculations.

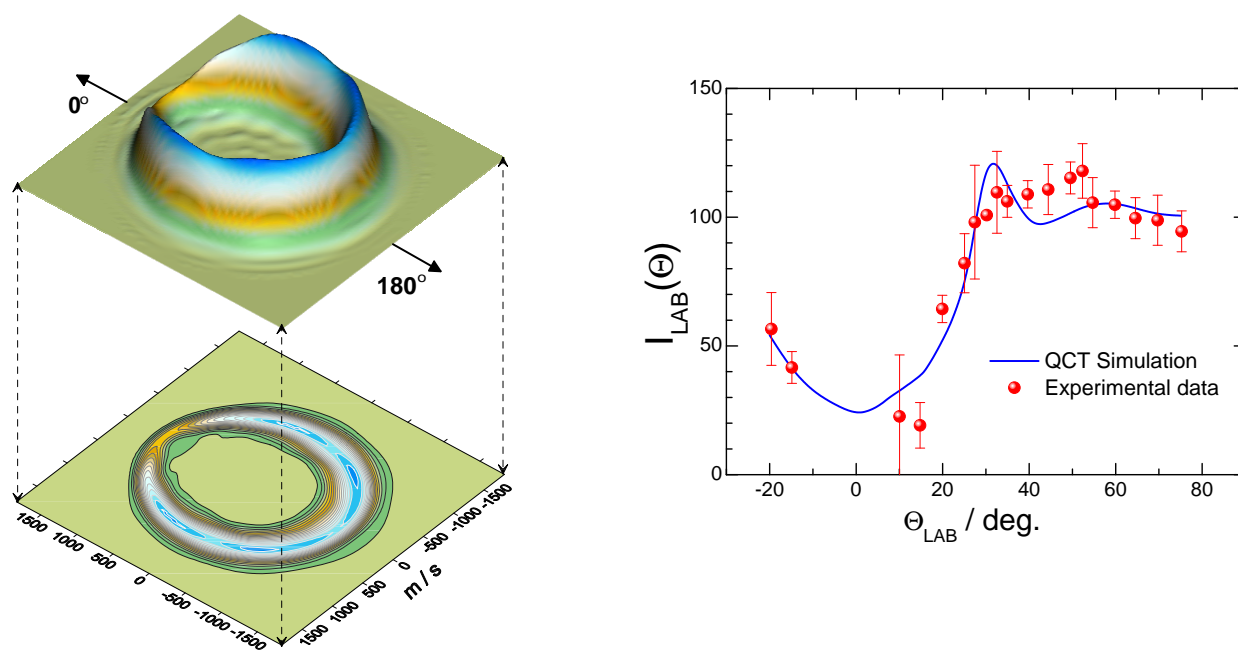


Fig. 6 Left panel: Three dimensional perspective and contour polar plots of the triple angle-velocity differential cross section for the $\text{Cl} + \text{O}_3 \rightarrow \text{ClO} + \text{O}_2$ reaction at the nominal (fixed) collision energy $E_T = 6 \text{ kcal mol}^{-1}$. Right panel: Comparison of the experimental and simulated ClO product LAB AD. The solid circles stand for the experimental data, and the solid line represents the simulated LAB AD at $E_{\text{coll}} = 5.85 \text{ kcal mol}^{-1}$ mean collision energy (6 kcal mol^{-1} nominal collision energy) using the QCT results calculated varying the collision energy and using eqn (7).

The CM polar plot and the 3D perspective of the angle-velocity polar map at 6 kcal mol^{-1} nominal collision energy are represented in the left panel of Fig. 6. At this collision energy the ClO products are scattered almost isotropically except in the forward direction defined by the incoming velocity of the Cl atom. As commented on above, the transition state is such that the ClO can be scattered in any direction except at small angles in the forward region where there is some hindrance since is occupied by the O_2 molecule. In addition, the products are scattered with recoil velocities in the range from 1450 m s^{-1} to 600 m s^{-1} , with a mean value of $0.6 \times w'_{\text{max}}(E_T) \approx 1090 \text{ m s}^{-1}$, where $w'_{\text{max}}(E_T)$ is the maximum (nominal) recoil velocity compatible with the energy conservation, shown in Table 2. The inspection of the polar plot evinces the coupling of angular and the recoil velocity; that is, the recoil velocity distribution varies with the scattering angle. This can be clearly seen when comparing the forward and

backward velocity distributions: the peak velocities are 1300 m s^{-1} and 1050 m s^{-1} at $\theta=0^\circ$, and 180° , respectively. This variation is however relatively mild compared to that of most atom-diatom direct reactions.

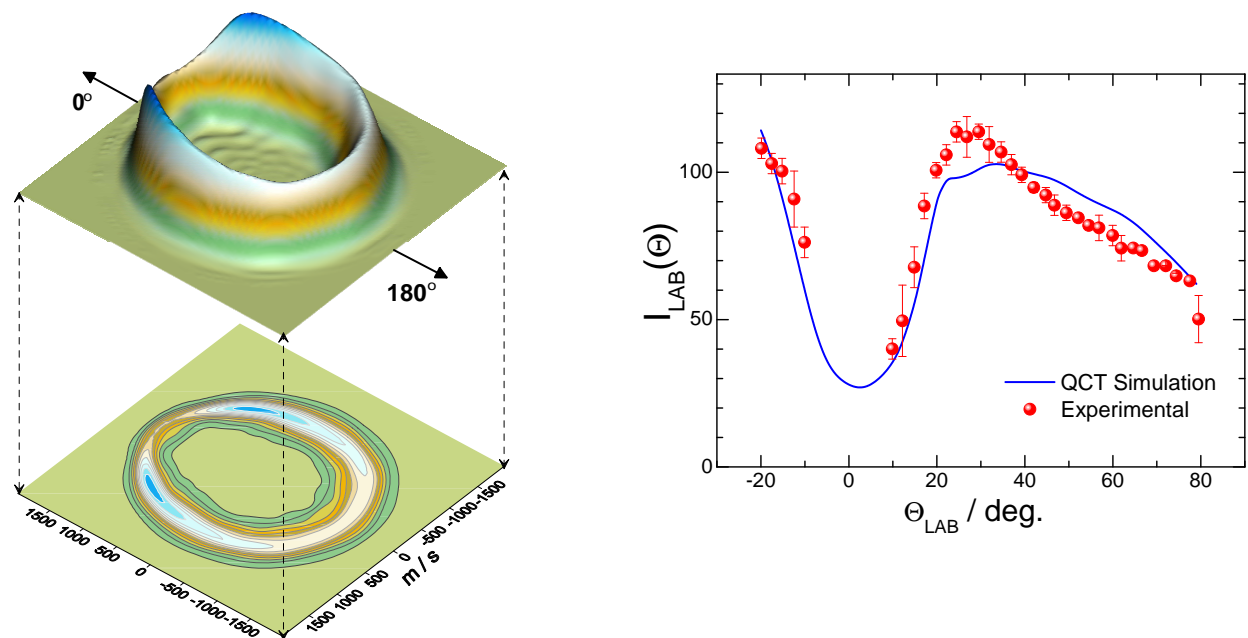


Fig. 7 Left panel: Same as Fig. 6 but at the nominal (fixed) collision energy $E_T = 13.5 \text{ kcal mol}^{-1}$. Right panel: Comparison of the experimental and simulated ClO product LAB AD. The solid circles stands for the experimental data, and the solid line represents the simulated LAB AD at $E_{\text{coll}} = 13.65 \text{ kcal mol}^{-1}$ mean collision energy ($13.5 \text{ kcal mol}^{-1}$ nominal collision energy) using the QCT results calculated varying the collision energy and using eqn (7).

In the experimental article,¹⁰ the authors derived an angle-velocity polar map at each of the three collision energies at which the measurements were carried out. The ‘experimental’ AV-DCSs were fitted by comparing the forward convolution with the data obtained in the LAB frame. The polar map at 6 kcal mol^{-1} nominal collision energy depicted in Fig. 6 is in very good agreement with that derived from the experimental data (see Fig. 13 of ref. 10). The effect of the distributions shifting to higher values of the recoil velocity from backward to forward scattering was also found in the experimental derivation of the CM AV distributions.

Inserting the AV distribution as a function of the collision energy, given by eqn (7) into eqn (17) and using the experimental conditions and beam parameters, we have simulated the LAB AD. The right panel of Fig. 6 depicts the comparison of the simulation with the measured values. The agreement is rather satisfactory considering that no adjustable parameter has been used in the simulation. The main discrepancies occur at $\Theta_{\text{LAB}} = 40\text{-}50^\circ$ for which the calculation predict somewhat less signal than that found experimentally.

Similar treatment has been carried out at $13.5 \text{ kcal mol}^{-1}$ nominal energy. The theoretical AV polar map calculated at this collision energy is shown in the left-hand side of Fig. 7. As can be seen, the angular distribution is less isotropic:

scattering in the 30-60° angular range has increased considerably with respect to what was found at lower energies. The theoretical map is in very good agreement with that shown in Fig. 10 of ref. 10. As for the lowest energy, the LAB AD was simulated using the theoretical results. The right panel of Fig. 7 shows the comparison between simulated and experimental data. The theoretical curve reproduces the overall shape of the experimental data although underestimates the scattering in the $\Theta_{\text{LAB}}=20\text{-}30^\circ$ angular range in the LAB frame. In contrast, for higher LAB angles, the theoretical curve overestimates the scattering in the LAB frame slightly. Taking into account the correspondence between the CM and LAB frames in which $\Theta_{\text{LAB}}=0^\circ$ almost coincides with the CM $\theta=0^\circ$, it becomes clear that the theoretical result predicts a too low scattering in the 20°-60° CM angular range that corresponds to the bulge that can be observed in the representation of the DCS as a function of the collision energy.

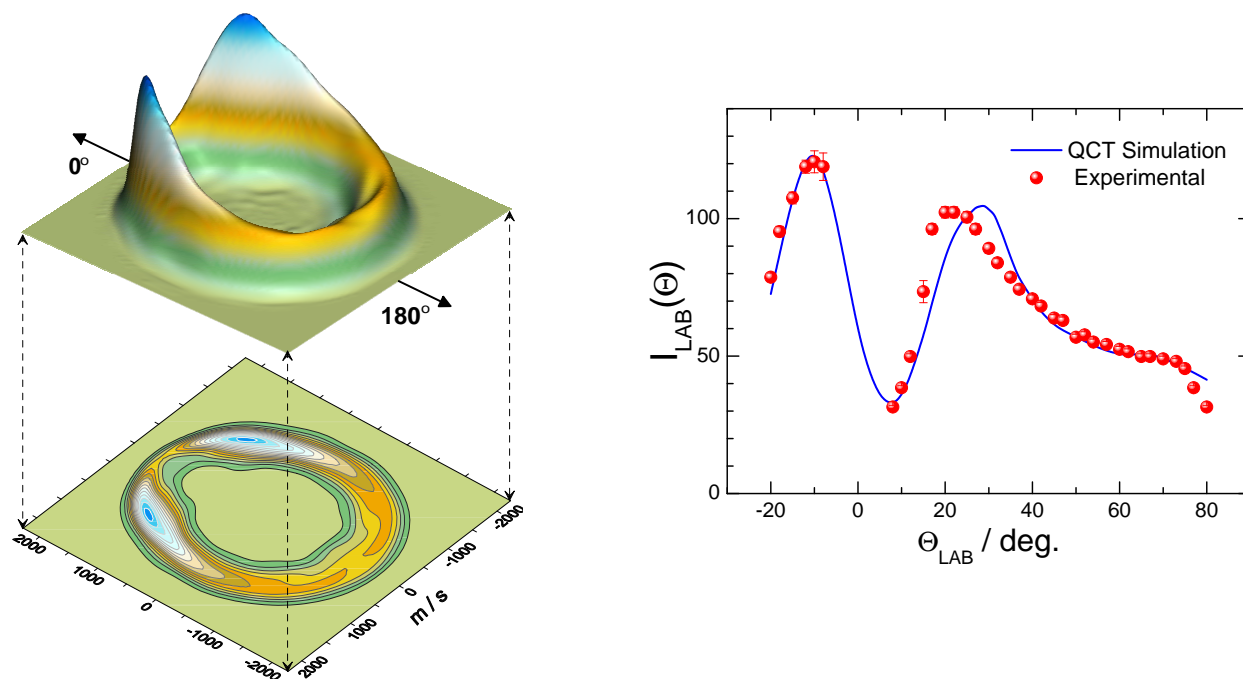


Fig. 8 Left panel: CIO Scattering angle-recoil velocity at $E_{\text{coll}} = 32.45 \text{ kcal mol}^{-1}$ (nominal energy $32.0 \text{ kcal mol}^{-1}$). Right panel: CIO LAB AD at the same collision energy. Solid points: experimental results. The line is the simulation using the QCT AV polar maps as a function of the collision energy.

The calculated TAV polar map at the 32 kcal mol^{-1} fixed collision energy is shown in the left panel of Fig. 8. This is the highest collision energy measured by Zhang and Lee.¹⁰ The major effect with increasing E_{T} is the rise of scattering in the 30–60° range of scattering angles as shown in Fig. 4. This feature manifests in the TAV polar map as two prominent ears in forward scattering and a considerable release of product translational energy. As in previous cases, there is a fairly good agreement with the polar map experimentally derived. The resulting simulation of the LAB AD at this nominal energy is displayed in the right-hand side of Fig. 8. Once again, the agreement with the experimental results is very satisfactory. In the 30–60° range of LAB scattering angles the simulated results are somewhat displaced towards higher Θ_{LAB} values. This discrepancy is also reflected in the experimentally derived polar map, where the ‘ears’ show up at angles closer to the forward direction, $\theta \approx 25\text{--}35^\circ$, somewhat smaller than

those of the maximum in the QCT results.

It must be pointed out that in all the simulations the translational (collision) energy dependence of the TAV-DCS has been taken into account, although the polar maps shown in each case correspond to those obtained at the mean collision energy of the experiments.

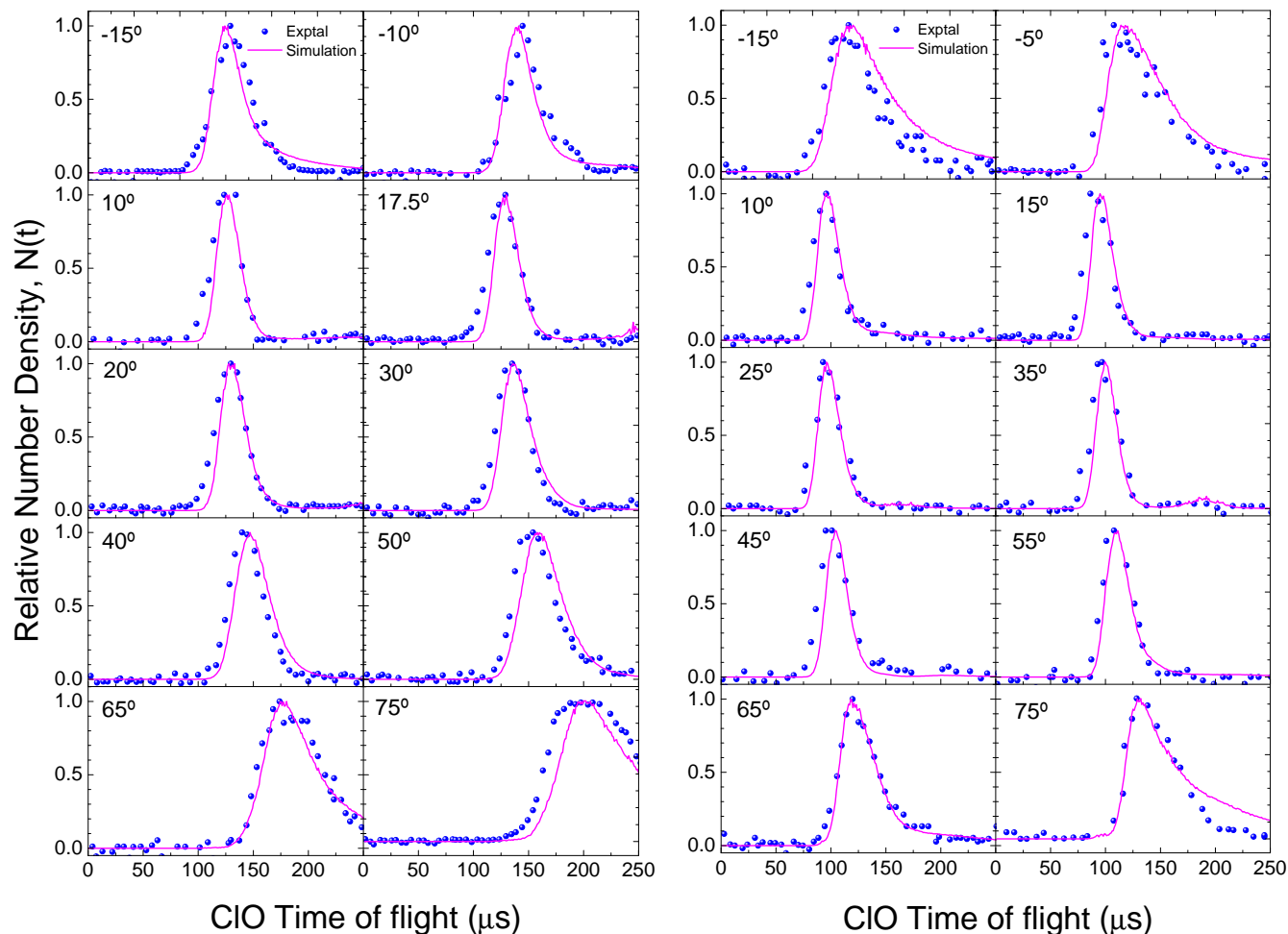


Fig. 9 CIO product's TOF spectra at the indicated LAB angles at $13.65 \text{ kcal mol}^{-1}$ mean collision energy ($13.5 \text{ kcal mol}^{-1}$ nominal energy) (left panel) and at $32.45 \text{ kcal mol}^{-1}$ mean collision ($32.0 \text{ kcal mol}^{-1}$ nominal energy) (right panel). The lines are the results of the simulation using the QCT results calculated varying the collision energy in the $1\text{--}56 \text{ kcal mol}^{-1}$ range. The (blue) points represent the experimental measurements

With the sole measurement of LAB ADs is practically impossible to derive accurate CM TAV-DCSs. This requires the additional measurement of the LAB velocities, usually in the form of TOF spectra. To extract the CM angular and recoil velocity distributions in ref. 10, the TOF spectra at the various collision energies were measured and those corresponding to $13.5 \text{ kcal mol}^{-1}$ and $32.0 \text{ kcal mol}^{-1}$ were also reported in that article for a series of LAB angles. A further assessment of the present theoretical approach consists in the simulation of the TOF and their comparison with the experimental data. The simulation using the present QCT results in the CM has been carried out with the procedure described in Section 3.1, consisting in evaluating the integral of eqn (18) with Monte Carlo sampling,

taking into account the instrumental functions and the beam characteristics. The results at the two mentioned energies are plotted in Fig. 9, where the simulations are compared with the experimental data. The overall agreement is very satisfactory with minor discrepancies at some of the measured angles. The good accordance between the experimental and theoretically simulated TOFs lends credence to the QCT characterization of the dynamics of this reaction on the CAM10 PES.

4 Discussion

One of the most interesting features of the evolution of the DCSs with the collision energy is the emergence of the bulge at 40° - 60° that appears as an “ear” in the TAV DCS. This structure becomes particularly prominent above ≈ 15 kcal mol $^{-1}$. In order to shed light on its origin, the relation between the scattering angle and the impact parameter (or the orbital angular momentum) can be shown by means of the normalized deflection function, $D_r(\ell, \theta)$, as given by eqn (21). Figs. 10 and 11 represent the deflection functions as gradational contour maps at 6 kcal mol $^{-1}$ and 32 kcal mol $^{-1}$, respectively. The right and left scale represent the orbital angular momentum and impact parameter, respectively. Comparing the two figures, it is noticeable that, with increasing E_T , the range of impact parameters that give rise to reactive scattering diminishes. This decrease however does not compensate for the increase of collision energies, and the range of ℓ values are considerably larger at 32 kcal mol $^{-1}$ with a maximum value $\ell_{\max} \approx 350$.

The more conspicuous characteristic is the correlation between ℓ (or b) and θ . As a general rule, the larger ℓ is, the more forward is the scattering angle, following a pattern shape that goes diagonally across the $\ell - \theta$ plane. This correlation, however, is fairly loose, encompassing broad distributions of both ℓ and θ . In addition, this behaviour, and hence the qualitative shape of the deflection function, does not change significantly with E_T , even below the minimum of the excitation function, ruling out the appearance of a different mechanism. At the selected energies of Figs. 10 and 11, it is remarkable that the lowest impact parameters do not give rise to the most backward scattering. As can be seen, scattering in the 170 - 180° is caused by impact parameter above 0.5 Å. The lowest impact parameters, $b \leq 0.2$ Å contribute to scattering in the 120 - 160 range. In spite of the similarities, the deflection function at 6 kcal mol $^{-1}$ is much wider with a broad and diffuse maximum covering the 50° - 100° and impact parameters from 1 Å to 2.5 Å, $\ell \in [50, 120]$. With increasing collision energy, the deflection function becomes narrower with a sharp and well localized maximum at impact parameters between 2 and 2.5 Å (or ℓ values in the 220 - 290 range). This maximum in the region 30° - 60° corresponds to the bulge observed in the DCS, which also shows up in the LAB AD. The deflection function becomes wider for smaller impact parameters, adopting a characteristic fin-shape.

Complementary to the deflection function shown in Fig. 11, we have calculated the build-up of the DCS with increasing contributions from impact parameters at 32 kcal mol $^{-1}$, which is shown in Fig. 12 (without being multiplied by $\sin \theta$). Some interesting features are obvious from the figure: (i) the lowest impact parameters, $b \leq 0.5$ Å, do not contribute to extreme backward scattering, (ii) backward scattering in the 120 - 180° arises exclusively from $b \leq 1.5$ Å, (iii) in turn, forward scattering, $\theta < 30^\circ$ is caused by collisions with $b \geq 2$ Å, and (iv) the maximum in the DCS, that leaves a clear imprint in the LAB AD and TAV-DCS, is due to collisions with $b > 2.3$ Å.

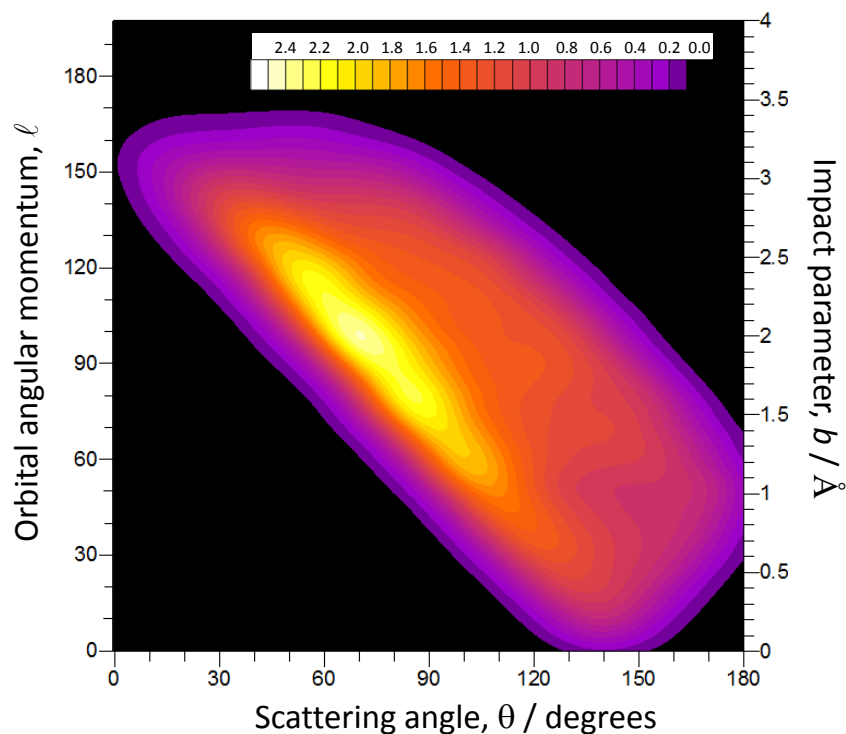


Fig. 10 Gradational contour map representing the normalized classical deflection function, $D_r(\ell, \theta)$, as defined by eqn (21), at $5.85 \text{ kcal mol}^{-1}$ mean collision ($6.0 \text{ kcal mol}^{-1}$ nominal energy). The left and right scales are for orbital angular momentum and impact parameter, respectively.

5 Conclusions

In this work we have studied in detail the dynamics of the $\text{Cl}+\text{O}_3$ reaction in the $1\text{-}56 \text{ kcal mol}^{-1}$ range. The main goal of this work has been to assess the accuracy of the recent CAM10 PES by Castillo *et al.* and the reliability of QCT calculations to reproduce the crossed molecular beam results by Zhang and Lee. Therefore, this work is aimed at simulating the observables in the laboratory frame using QCT calculations on the just mentioned CAM10 PES. Given the relatively broad experimental collision energy distributions, an accurate simulation of the laboratory measurements requires to take into account the energy dependence of the theoretical angle-velocity distributions in the centre-of-the-mass (CM) frame, especially considering that both the value of the integral cross section and the angle-velocity distributions (polar maps) change considerably in the range of collision energies spanned by the experiment.

To fulfill this requirement, we have developed a general QCT methodology to determine integral and differential cross sections, recoil velocity distributions, and triple scattering angle-recoil velocity polar maps, all of them as a continuous function of the collision energy. For this purpose, trajectories have been run by varying randomly the collision energy for each trajectory and selecting the maximum impact parameter at each energy. The various magnitudes

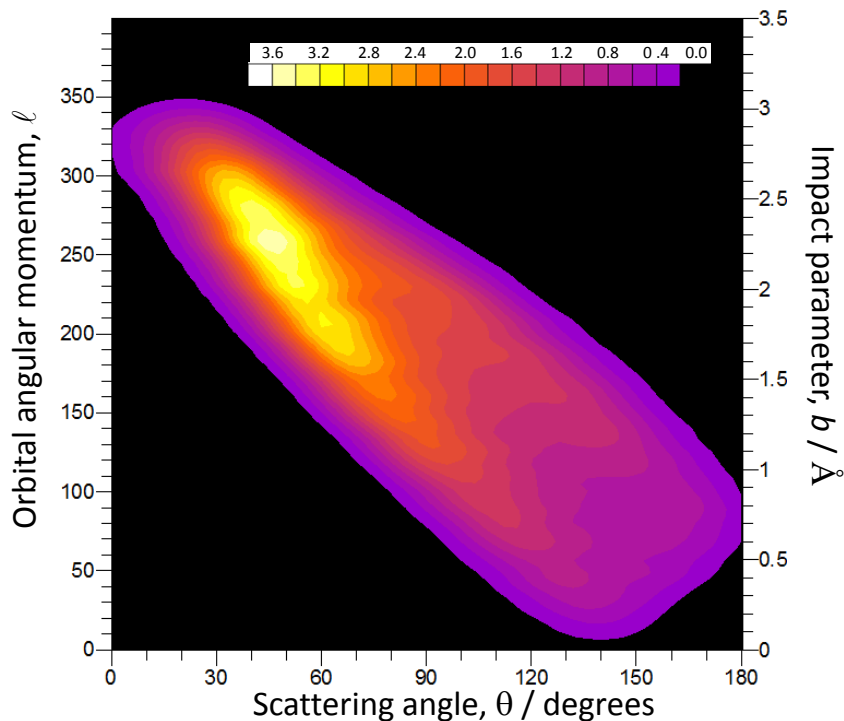


Fig. 11 Same as figure 10 but at $32.45 \text{ kcal mol}^{-1}$ mean collision (32 kcal mol^{-1} nominal energy). Notice that although the range of impact parameters is smaller than in Fig. 10, the range of orbital angular is almost twice due to the larger collision energy.

have been determined by using the method of double and triple moment expansions in Legendre polynomials whose arguments are the reduced variables of the collision energy, scattering angle and recoil velocity. The results obtained using the ensemble of collision energy dependent trajectories for a selected specific energy have been shown to be in excellent agreement with those calculated at fixed collision energy. The method has been shown to be very robust, easily to implement for the simulation in the laboratory frame and computationally less costly than running trajectories at a sufficiently fine grid of energies. The method of the triple fit is ideally suited for QCT calculations without resolution in quantum states of the products as is the case of the above mentioned cross molecular beam experiment.

The QCT collision energy dependent CM joint angle-velocity distributions (including the cross section dependence) have been used to simulate the angular distribution and time-of-flight spectra in the laboratory frame at each of the three collision energies reported in the article by Zhang and Lee. The agreement has been found to be very good in all cases, except for relatively small discrepancies in the laboratory angular distributions, which can be traced to a slight underestimation of the size of the peak in the forward region in the QCT differential cross section. A very good accordance was also found in the comparison between the experimentally derived magnitudes with those calculated by QCT, in particular in the case of angle-velocity polar maps. This agreement gives credence to the QCT method ap-

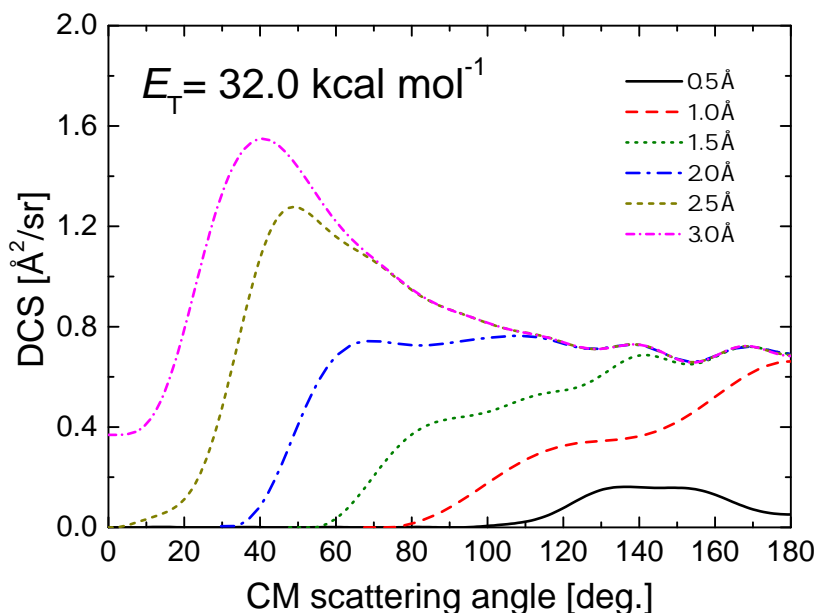


Fig. 12 Build up of the DCS at 32 kcal/mol. In each case, the DCS is made with contributions of impact parameters from zero to the indicated value of b in the figure.

plied to this reaction and to the reliability of the PES. This is remarkable considering that for a four-atom reaction only 800 *ab initio* points were necessary to converge the PES. These facts, on the other hand, are not completely surprising taking into account that the reaction is strongly exothermic, essentially barrierless, and with a very early transition state that resembles the Cl–O₃ asymptote. Moreover, it was shown in a previous work¹² that the zero point energy does not change much along the whole reaction path, hence minimizing the problem of the zero point energy leaking. All these characteristics underpin the use of the QCT approximation, and makes possible to construct a reliable PES based on relatively few *ab initio* points.

It can be objected that the good performance of the QCT results on the CAM10 PES may be due to a lucky cancellation of errors. However, the very good agreement of the experimental rate coefficients in the 200–300 K temperature range with those calculated using the Ring Polymer Molecular Dynamics Method (RPMD), which is considered to be very accurate, close to exact quantum calculations, on the CAM10 seems to further demonstrate the adequacy of this PES. The lower values of the QCT rate coefficients at $T < 300 \text{ K}$ with respect to the experimental values or to those calculated with the RPMD method are likely to be attributed to a poor extrapolation of the rotationally averaged excitation functions at energies below 1 kcal mol^{-1} . Clearly, more QCT calculations would be needed at those small collision energies.

Finally, the features found in the DCS, angle-velocity polar maps, which are reflected in the laboratory frame magnitudes, have been analysed using the classical reactive deflection functions (the scattering angle-impact parameter joint distributions). This analysis rules out the presence of long-lived collision complexes and predict that interferences can only take place between relatively close partial waves. Those coherences are expected to show up only for state-resolved DCSs and would be blurred by summing over final states.

It would be desirable to perform QM calculations for this reaction. However, such a task does not seem feasible in the short term, not only for involving four heavy atoms, small rotational and vibrational energy spacing of the reagents and products, but also for the huge number of partial waves that would be necessary for the convergence of the calculations (above $\ell=350$ at 32 kcal mol^{-1} , as shown in Fig. 11). Fortunately, in this case, the QCT approach seems to be a trustworthy approximation to describe the existing experimental data.

6 Acknowledgments

Funding by the Spanish Ministries of Science and Innovation and Economy and Competitiveness (grants CSD2009-00038, and CTQ2012-37404-C02) are gratefully acknowledged.

References

- 1 M. J. Molina and F. S. Rowland, *Nature*, 1974, **249**, 810–812.
- 2 S. P. Sander, J. Abbatt, J. R. Barker, J. B. Burkholder, R. R. Friedl, D. M. Golden, R. E. Huie, C. E. Kolb, M. J. Kurylo, G. K. Moortgat, V. L. Orkin, and P. H. Wine, *Chemical Kinetics and Photochemical Data for Use in Atmospheric Studies, Evaluation No. 17. JPL Publication 10-6*, Jet Propulsion Laboratory, Pasadena, 2011.
- 3 M. von Hobe, R. J. Salawitch, T. Canty, H. Keller-Rudek, G. K. Moortgat, J.-U. Grooss, R. Mueller, and F. Stroh, *Atmos. Chem. Phys.*, 2007, **7**, 3055–3069.
- 4 T. Rathmann and R. Schindler, *Chem. Phys. Lett.*, 1992, **190**, 539–542.
- 5 A. Rauk, E. Tschuikow-Roux, Y. Chen, M. P. McGrath, and L. Radom, *J. Phys. Chem.*, 1993, **97**, 7947–7954.
- 6 D.-Y. Hwang and A. M. Mebel, *J. Chem. Phys.*, 1998, **109**, 10847–10852.
- 7 J. Tyrrell, T. Kar, and L. J. Bartolotti, *J. Phys. Chem. A*, 2001, **105**, 4065–4070.
- 8 S. C. Farantos and J. N. Murrell, *Int. J. Quant. Chem.*, 1978, **14**, 659–674.
- 9 M. Zahniser, F. Kaufman, and J. Anderson, *Chem. Phys. Lett.*, 1976, **37**, 226–231.
- 10 J. Zhang and Y. T. Lee, *J. Phys. Chem. A*, 1997, **101**, 6485–6495.
- 11 J. F. Castillo, F. J. Aoiz, and B. Martínez-Haya, *Phys. Chem. Chem. Phys.*, 2011, **13**, 8537–8548.
- 12 R. Pérez de Tudela, Y. V. Suleimanov, M. Menéndez, J. F. Castillo, and F. J. Aoiz, *Phys. Chem. Chem. Phys.*, 2014, **16**, 2920–2927.
- 13 M. A. Collins, *Theor Chem Acc*, 2002, **108**, 313–324.
- 14 Y. V. Suleimanov, R. Colleparado-Guevara, and D. E. Manolopoulos, *J. Chem. Phys.*, 2011, **134**(4), 044131.
- 15 Y. V. Suleimanov, J. W. Allen, and W. H. Green, *Comput. Phys. Commun.*, 2013, **184**(3), 833–840.
- 16 F. J. Aoiz, L. Bañares, T. Díez-Rojo, V. J. Herrero, and V. Sáez Rábanos, *J. Phys. Chem.*, 1996, **100**, 4071.
- 17 F. J. Aoiz, L. Bañares, V. J. Herrero, V. Sáez Rábanos, and I. Tanarro, *J. Phys. Chem. A*, 1997, **101**, 6165.
- 18 J. F. Castillo, F. J. Aoiz, L. Bañares, and M. A. Collins, *J. Phys. Chem. A*, 2004, **108**, 6611.
- 19 M. J. T. Jordan, K. C. Thompson, and M. A. Collins, *J. Chem. Phys.*, 1995, **102**, 5647–5657.
- 20 K. C. Thompson, M. J. T. Jordan, and M. A. Collins, *J. Chem. Phys.*, 1998, **108**, 8302–8316.
- 21 R. P. A. Bettens and M. A. Collins, *J. Chem. Phys.*, 1999, **111**, 816–826.
- 22 W. L. Hase and et al., *QCPE*, 1996, **16**, 671.
- 23 F. J. Aoiz, L. Bañares, and V. J. Herrero, *J. Chem. Soc. Faraday Trans.*, 1998, **94**, 2483.
- 24 F. J. Aoiz, E. Verdasco, V. Sáez Rábanos, H.-J. Loesch, M. Menéndez, and F. Stienkemeier, *Phys. Chem. Chem. Phys.*, 2000, **2**, 451.
- 25 F. J. Aoiz, V. J. Herrero, and V. Sáez Rábanos, *J. Chem. Phys.*, 1992, **97**, 7423–7436.
- 26 F. J. Aoiz, L. Bañares, B. Martínez-Haya, J. F. Castillo, D. E. Manolopoulos, K. Stark, and H.-J. Werner, *J. Phys. Chem. A*, 1997, **101**, 6403.
- 27 F. J. Aoiz, E. Verdasco, V. Sáez Rábanos, H. Loesch, M. Menéndez, and F. Stienkemeier, *Phys. Chem. Chem. Phys.*, 2000, **2**, 541.

- 28 F. J. Aoiz, L. Bañares, V. J. Herrero, V. Sáez Rábanos, K. Stark, and H. Werner, *J. Chem. Phys.*, 1995, **102**, 9248.
- 29 R. Bobbenkamp, A. Paladini, A. Russo, H.-J. Loesch, M. Menéndez, E. Verdasco, F. J. Aoiz, and H.-J. Werner, *J. Chem. Phys.*, 2005, **122**, 244304.